Response of Evapotranspiration (ET) to Climate Change and Human Activities in the Shiyang River Basin, Northwestern China

Xueyi Yang , Xiaojing Shi , Yaling Zhang , Fei Tian * , Samuel Ortega-Farias

Posted Date: 21 June 2023

doi: 10.20944/preprints202306.1518.v1

Keywords: planting structure; evapotranspiration; remote sensing; climate change

Article

Response of Evapotranspiration (ET) to Climate Change and Human Activities in the Shiyang River Basin, Northwestern China

Xueyi Yang [1,2], Xiaojing Shi [1,2], Yaling Zhang [1,2], Fei Tian [1,2,*] and Samuel Ortega-Farias [3]

[1] Center for Agricultural Water Research in China, China Agricultural University , Beijing 100083, China; 1126sherry2021@gmail.com(X.Y.);xiaojing06009@gmail.com(X.S.);zhangyl_20@163.com（Y,Z）
[2] National Field Scientific Observation and Research Station on Efficient Water Use of Oasis Agriculture in Wuwei of Gansu Province, Wuwei 733000, China
[3] Research Program on Adaptation of Agriculture to Climate Change (A2C2), Research and Extension Center for Irrigation and Agroclimatology (CITRA), Faculty of Agricultural Sciences, Universidad de Talca, Campus Talca, Talca 3460000, Chile; sortega@utalca.cl
* Correspondence: feitian@cau.edu.cn; Tel.: +86-010-6273-6273

Abstract: Evapotranspiration (ET) is an essential part of energy flow between the surface of the earth and the atmosphere, simultaneously involving the water, carbon, and energy cycles. It is mainly determined by climate change, land use, and land cover changes. Climate change is expected to intensify the hydrological cycle and alter ET. Land use affects ET within regional ecosystems mainly through vegetation changes and agricultural activities such as farmland reclamation, crop cultivation, and agricultural management. However, there is still a need for quantitative characterization of the impacts of climate change and human activities on ET and regional water resource efficiency in arid and semiarid regions. Based on Landsat-8 remote sensing imagery and land use data, the planting structure in the Liangzhou District of the middle reaches of the Shiyang River Basin was identified using a multiband and multitemporal approach in this study. Subsequently, the ET of major cash crops was inverted using the three-temperature model. This research quantitatively describes the responses of wheat and corn to the climate and human activities over a two-year period. Furthermore, the impact of planting structure and climatic factors on ET was elucidated. The results indicate that a combination of multitemporal green and shortwave infrared 1 bands is the optimal spectral combination to extract the planting structure. Compared to 2019, the wheat area decreased by 23.27% in 2020, while the corn area increased by 5.96%. Both crops exhibited significant spatial heterogeneity in ET during the growing season. The typical daily range of ET for wheat was 0.4–7.2 mm/day, and for corn, it was 1.5–4.0 mm/day. Among the climatic factors, temperature showed the highest correlation with ET (R = 0.80, $p \leq 0.05$). Our research findings provide valuable insights for the fine identification of planting structures and a better understanding of the response of ET to climatic factors and human activities.

Keywords: planting structure; evapotranspiration; remote sensing; climate change

1. Introduction

Evapotranspiration (ET) is a crucial component of surface energy balance and water balance, consisting of soil evaporation and vegetation transpiration. It returns 58%–65% of terrestrial precipitation to the atmosphere and transports 51%–58% of surface energy from land through latent heat transfer [1,2]. Simultaneously, ET is regarded as the most important aspect of agricultural water allocation, with more accurate parameter values leading to more optimized farmland water strategies [3]. Traditional ET, primarily based on observations at stations, is obtained through point-scale field measurements, making it difficult to acquire regional-scale ET. However, remote sensing technology, with its wide coverage, periodicity, and timeliness, can effectively obtain large-scale ET [4]. Remote

sensing-based ET estimation methods overcome the limitation of "point" observation. By using satellite sensors with high spatial and temporal resolution to obtain surface reflectance and combining it with multispectral, hyperspectral, and thermal infrared sensors on unmanned aerial vehicle platforms, the accuracy of the ET estimation model can be effectively improved at the regional level. For instance, the three-temperature model (3T model) proposed by Qiu et al. [5,6] can effectively estimate ET and its components. The model requires fewer input parameters, which can be obtained through remote sensing inversion or meteorological stations. This model has been successfully applied for the quantitative characterization of ET at various scales in the northwest arid zone [7–9].

ET itself is affected by a variety of factors, such as crop type, crop growing conditions, soil conditions, and the climate. However, changes in ET are mainly determined by climate change, land use, and land cover change [10]. Regarding the driving mechanism of crop ET, the impact of climate change and human activities on ET has been a hot topic in the process of the terrestrial hydrological cycle [11–14]. Jin et al. [15] used the ET model to separate the effects of vegetation restoration and climate change on ET by controlling variables and found that vegetation restoration was the main driver of ET increase; He et al. [16] analyzed precipitation, potential ET, and ET based on the Budyko equation. They found that based on the average impact of vegetation restoration on ET changes, precipitation was the main driving factor for the ET changes. ET inversion and the hydrological models used by the above scholars can effectively evaluate the impact of climate and vegetation changes on ET changes. Still, there exist few studies on the effects of crop planting structure changes on ET under the broken and complex planting structure.

Identifying crop planting structures is vital to efficiently using agricultural water resources and supporting food security. The accurate monitoring of farmland information is also one of the central themes of agricultural remote sensing [17–19]. The classification of land use types in existing research has primarily been macroscopic, mainly divided into forestland, grassland, cultivated land, and urban land. However, most of the Liangzhou District (LD) focuses on developing agriculture, and there needs to be more quantitative research on the impact of different crop types on regional ET changes. Remote sensing data contains rich spectral geometry and texture features, which can distinguish the phenological characteristics, leaf pigment, leaf water content, and canopy structure of different crops so that the unique spectral reflection characteristics of other crops can be used to identify the planting structure [20].

The method of crop identification using remote sensing data has been updated and matured, and different satellite remote sensing images have their own advantages for crop identification at different temporal and spatial scales [21–26]. At the regional scale, high-resolution remote sensing data have shown better results for the identification of broken and complex planting structures [27–30]. Currently, crop remote sensing identification and classification methods can be distinguished based on the crop classification features and satellite image identification information used. The classification characteristics can mainly be divided into the following three categories: vegetation spectral information feature recognition [31], field texture feature recognition, and crop phenology information recognition [32]; meanwhile, the identification information can be divided into satellite image-based spectral information [33] and multitemporal information [34–36]. Using multisource remote sensing images (from Landsat-8 and Sentinel-2) based on supervised classification algorithms (the random forest algorithm and support vector machine algorithm) and an object-oriented segmentation algorithm (the recursive hierarchical segmentation algorithm), Xiong et al. [37] created a set of farmland distribution maps of 30 meters in Africa from 2003 to 2014, and the overall accuracy reached 94%. Based on the spatiotemporal data fusion model, Chen et al. [38] in the typical agricultural areas of Hebei, Heilongjiang, and Xinjiang, the major planting provinces in northern China, used Landsat and MODIS images to construct a high spatiotemporal resolution image data set to explore the applicability of the spatiotemporal data fusion model in the field of agricultural information extraction.

The Shiyang River Basin, situated in the arid region of Northwest China, experiences limited rainfall, significant ET rates, extensive water resource development, and a delicate natural ecology. Oasis farmland comprises approximately 10% of the total area in the Shiyang River Basin, with

 doi:10.20944/preprints202306.1518.v1

agricultural water being the foremost consumer of water resources within the basin. Irrigated agriculture is developed in the LD, which is located in the oasis area in the middle reaches of the river basin. The mismatch between the supply of and demand for agricultural water is the most prominent in this area. With the implementation of a water-saving reconstruction project, the ecological environment of the LD has been significantly improved, and the change in vegetation has had a direct or indirect impact on the regional hydrological cycle. Thus, under the combined effect of climate and planting structure changes, there is great significance to effectively evaluating the relative contribution rate of different influential factors on regional ET for the efficient use of water resources in the LD. However, the distribution of farmland in the LD has a certain complexity, with fragmented land plots and complex types. Therefore, it is necessary to find a method suitable for planting structure identification in the LD.

The objectives of this study are to (1) provide methods applicable to extracting typical crop planting structures in the middle reaches of the Shiyang River basin based on Landsat-8 high-resolution imagery, (2) quantitatively characterize the spatial and temporal variability of ET from typical crops under the influence of climate change and human activities based on the 3T model, and (3) investigate the driving factors of climate and planting structure for regional ET.

2. Materials and Methods

2.1 Study Area

The LD is located in Wuwei City, Gansu Province, Northwest China (101 59'-103 23'E, 37 23'-38 12'N), at the eastern end of the Hexi Corridor and the center of the Wuwei Oasis in the middle reaches of the Shiyang River Basin. The area is 5,081 square kilometers, and the agricultural land is about 2,155 square kilometers, accounting for 42.9% of the total area. The distribution of cropland in the study area is concentrated, and the area of farmland is relatively large. The terrain of this area is high in the southwest and low in the northeast, with an altitude of 1,440–3,263 meters (Figure 1). This region belongs to the temperate continental arid climate, which is dry, with little rainfall and large temperature differences between day and night. The LD has typical dryland climate characteristics, with an average annual temperature of 7.7°C, annual evaporation of 2,020 mm, and average annual precipitation of 100 mm, which is far from sufficient to supply water for agricultural development. The area has 2,873.4 h of sunshine and 139.05 kcal/cm^2 of total solar radiation. In recent years, the average temperature in the LD has exceeded the 1975–2015 average, making agricultural water use a more serious challenge in the context of climate change.

Preprints (www.preprints.org) | NOT PEER-REVIEWED | Posted: 21 June 2023 doi:10.20944/preprints202306.1518.v1

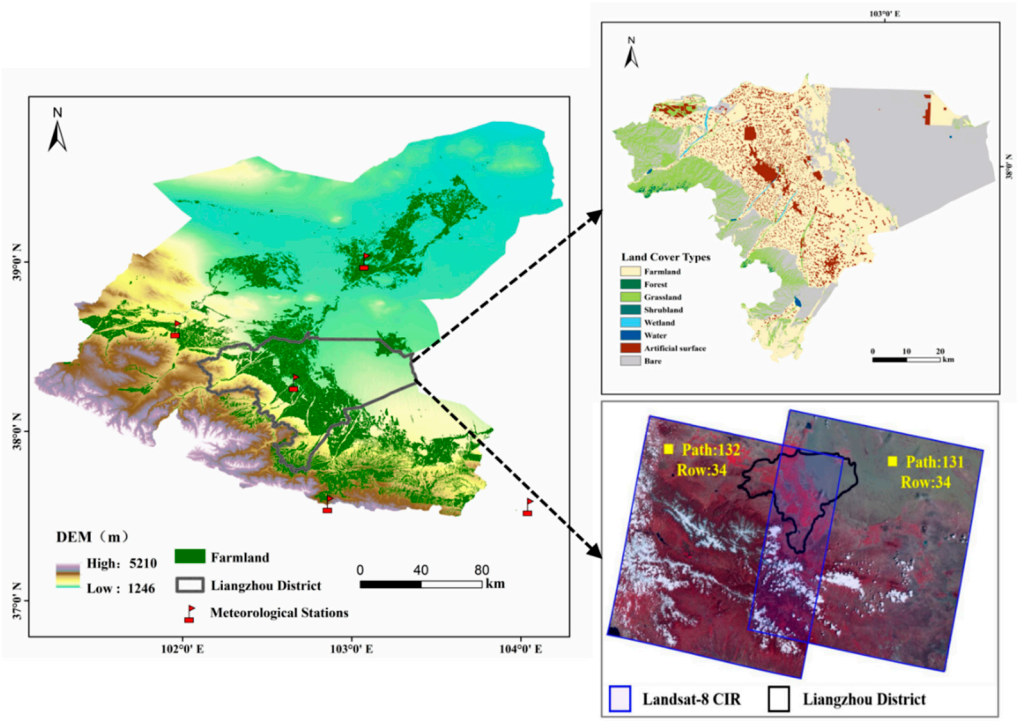

Figure 1. Study area of the Liangzhou District (LD).The LD is mosaicked by 2 Landsat-8 images.

The development of agricultural resources dominates the LD. The main food crops are wheat and corn, which account for over 60% of the cropped area. These two types of bulk food crops are the main water-consuming crops, and their growth period is from April to September. In the cultivated land, a portion of vegetable cultivation area accounts for 1% to 4% of the land. However, due to the diverse types of cash crops and small and fragmented plots, this study categorizes them collectively as vegetables. The phenological stages of crops in the study area are listed as follows (Table 1).

Table 1. Phenological information of crop types.

Crop Type	Apr.			May			Jun.			Jul.			Aug.			Sept.		
	E	M	L	E	M	L	E	M	L	E	M	L	E	M	L	E	M	L
Wheat	sow			grow				maturity			harvest							
Corn			sow					grow				maturity					harvest	
Veg.			sow											harvest				

2.2 Materials

2.2.1. Remote Sensing Data

Landsat-8 remote sensing images (Level 1T product, sourced from https://glovis.usgs.gov/) with a resolution of 30 m from NASA (the National Aeronautics and Space Administration) and the United States Geological Survey were used to collect satellite data, with a revisit period of 16 days. The acquired remote sensing data were first preprocessed, including radiometric calibration, atmospheric correction, and de-clouding. Then all available images for the crop birth period (April–September) with band numbers 131034 and 132034 were considered for selection (Table 2). Due to the large volume of clouds during this period, only dates with less cloud interference during the crop fertility period could be selected, resulting in a total of 15 days (Table 2). Six spectral bands (B2–B7) of the

Preprints (www.preprints.org) | NOT PEER-REVIEWED | Posted: 21 June 2023 doi:10.20944/preprints202306.1518.v1

Landsat-8 images, were classified as feature bands (Table 3) and used, including the blue, green, red, near infrared (NIR), shortwave infrared (SWIR) 1, and SWIR-2 bands. This study mainly focused on the farmland system, so a 30 m spatial resolution land use data mask was downloaded from the National Tibetan Plateau Scientific Data Center (http://data.tpdc.ac.cn/zh-hans/).

Table 2. Summary of Landsat-8 images used in 2019–2020.

Year	Date	Day of Year (DOY)	Path/Row	Transit Time
2019	May.12	132	132/034	11:49
	May.21	141	131/034	11:43
	May.28	148	132/034	11:49
	Jun.06	157	131/034	11:43
	Jun.13	164	132/034	11:49
	Jul.24	205	131/034	11:43
	Aug.09	221	131/034	11:43
	Aug.25	237	131/034	11:43
	Sept.01	244	132/034	11:49
	Sept.26	269	131/034	11:43
2020	Jun.24	176	131/034	11:43
	Jul.01	183	132/034	11:49
	Jul.10	192	131/034	11:43
	Jul.17	199	132/034	11:49
	Aug.18	231	132/034	11:49

Table 3. Detailed information of 6 spectral bands

Satellite	Band Name	Wavelength (nm)	Spatial Resolution (m)
Landsat-8 OLI	Blue	450-515	30
Landsat-8 OLI	Green	525-600	30
Landsat-8 OLI	Red	630-680	30
Landsat-8 OLI	NIR	845-885	30
Landsat-8 OLI	SWIR-1	1560-1660	30
Landsat-8 OLI	SWIR-2	2100-2300	30

2.2.2. Meteorological Data

Daily meteorological data including temperature (Ta), precipitation (P), and relative humidity (RH) were taken from the China Meteorological Data Network (http://data.cma.cn). Meanwhile, we gathered meteorological data from the meteorological stations around the LD (Table 4).

Table 4. General information about meteorological stations.

Station No.	Station Name	Longitude	Latitude	Altitude (m)
52681	Minqin	103°08′	38°63	1367.8
52674	Yongchang	101°97′	38°23	1976.9
52679	Wuwei	102°67′	37°92	1531.5
52787	Wushaoling	102°87′	37°02	3045.1

Preprints (www.preprints.org) | NOT PEER-REVIEWED | Posted: 21 June 2023 doi:10.20944/preprints202306.1518.v1

52797	Jingtai	104°05′	37°18	1630.9

Figure 2 shows data on climatic variables for the crop growing season. The monthly average precipitation during the growing season was 24.17 mm and 27.51 mm in 2019 and 2020, respectively. In 2019 the peak was at 51.40 mm in July, while in 2020 the peak was at 55.60 mm in September. The monthly temperatures during the growing season ranged from 11.45°C to 21.89°C, with a mean value of 17.75°C in 2019 and 17.85°C in 2020. Meanwhile, the annual mean value of the vapor pressure difference (VPD) showed an increasing trend, with the lowest value of 0.82 KPa occurring in September 2020 and the highest value of 1.57 KPa occurring in June of the same year. In general, variations in the meteorological data from the LD represent the typical seasonal trend in the northwest arid zone.

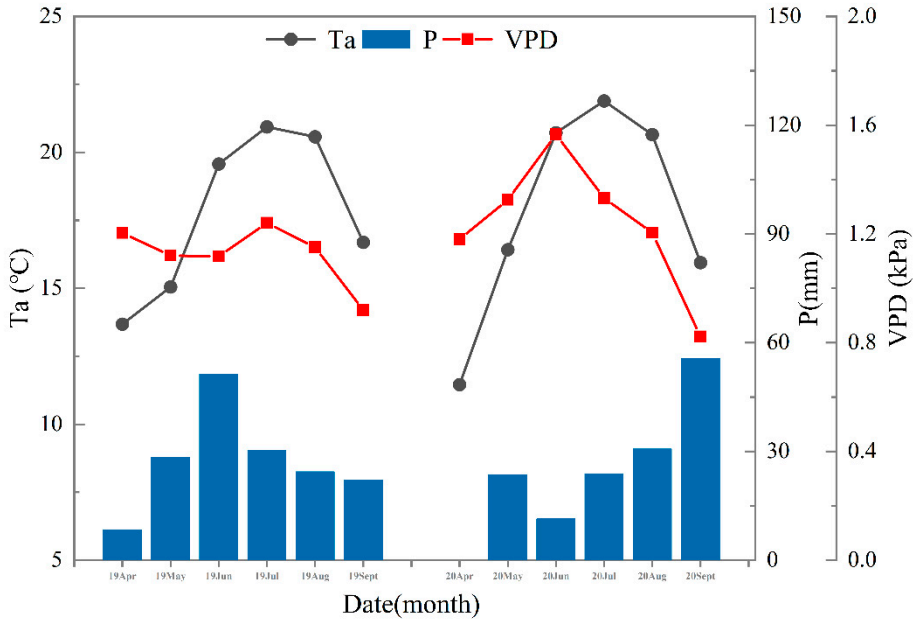

Figure 2. Monthly variations in temperature (Ta), precipitation (P), and vapor pressure difference (VPD) during the study period.

2.2.3. Sample Data

Sample plots were selected and identified to ensure the accuracy of crop classification by combining ground sampling points with the visual interpretation of high spatial resolution images on Google Earth Pro. During the experiment, a total of 247 sample plots were extracted in the study area, and a total of 5,632 pixels were used as ground truth datasets for model training and accuracy evaluation. The ground sampling points were randomly divided into two parts: 2/3 for model training and 1/3 for accuracy validation (Table 5).

Table 5. General information about the sample plots.

Crop Types	Number of Training Plots	Number of Testing Plots	Number of Training Pixels	Number of Training Pixels
Wheat	72	37	2384	665
Corn	96	42	3248	963

 doi:10.20944/preprints202306.1518.v1

2.3 Data Analysis

2.3.1. Crop Classification Method

Two classification experiments were designed to study and analyze the effects of different spectral bands and temporal combinations on crop classification results: First, for single-band multitemporal combinations, crop classification was performed using single-band analysis based on multitemporal conditions, which were mutually validated with the results from Experiment 2. Second, for multiband multitemporal combinations, the aim was to investigate how combinations of different wavebands affect the performance of a classification model under multitemporal conditions. The band combinations were categorized into five groups. The first group comprised two band combinations randomly selected from the B2–B7 bands of the Operational Land Imager (OLI) images, with a total of 15 combinations. The second group included three band combinations, totaling 20 combinations. The third group had four band combinations, with a total of 15 combinations. The fourth group comprised five band combinations with six possibilities. Finally, the fifth group included all bands in the OLI images, with only one combination. The classification effects of these 57 band combinations differed, allowing us to determine the sensitive bands and the best classification combinations for crop classification. Because the sensitivity of crops to different band combinations varies, this experiment can identify the optimal band combinations for effective crop classification. The accuracy of the classification experiments was evaluated by a confusion matrix. Random forest classification was conducted using two Python modules: pandas and scikit-learn. The classification process was designed to have good noise immunity by following the random and put-back principles during sampling.

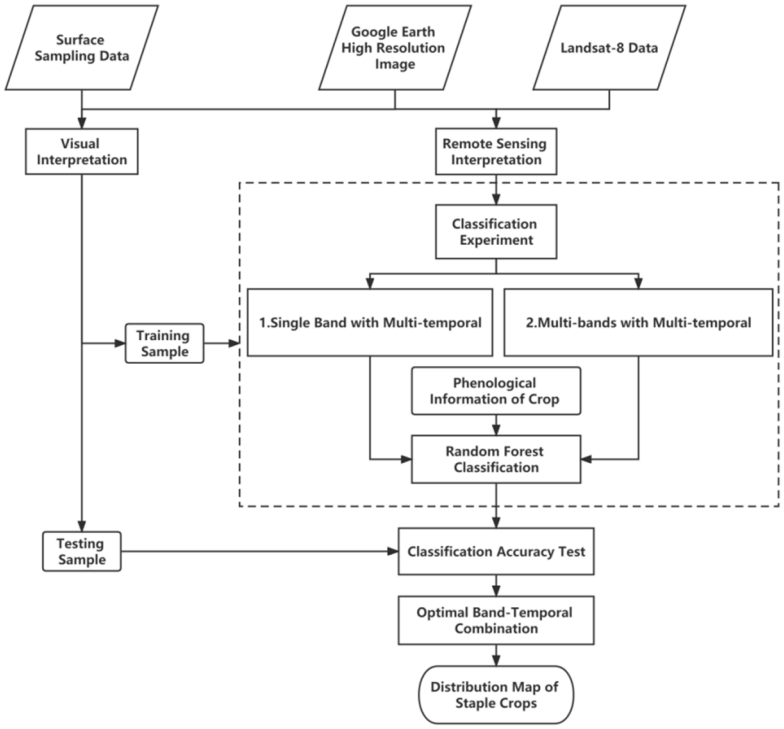

Figure 3. The workflow of crop classification using the random forest method.

2.3.2. Evapotranspiration Remote Sensing Estimation Method

The 3T model and satellite remote sensing images were employed in the study to calculate ET. Qiu et al. [5,6,39] proposed the 3T model to measure ET and evaluate environmental quality based on the surface energy balance equation in recent years. The model's input parameters are three temperatures, net radiation, and soil heat flux, with all parameters except air temperature being

Preprints (www.preprints.org) | NOT PEER-REVIEWED | Posted: 21 June 2023 doi:10.20944/preprints202306.1518.v1

obtainable by direct inversion of remote sensing data. The 3T model consists of two submodels: the soil evaporation submodel and the vegetation transpiration submodel. For the mixed zone of vegetation and soil, the model assigns weights to soil evaporation and vegetation transpiration according to the vegetation cover values and calculates the total transpiration. This model has been widely used in arid and semiarid regions and has yielded favorable results in the northwest dry zone [40,41].

Submodel of Soil Evaporation

When the surface is bare soil, the reference soil temperature (the temperature of dry soil with zero water evaporation) is introduced to calculate soil evaporation:

$$\lambda E = R_{n,s} - G_s - (R_{n,sd} - G_{sd})\frac{T_s - T_a}{T_{sd} - T_a}, \quad (1)$$

where λE_s is the latent heat flux of soil evaporation (W·m^{-2}), λ is the latent heat of the vaporization of water vapor, and E_s is soil evaporation. $R_{n,s}$ is the net radiation flux of the surface (W·m^{-2}), G_s is the soil heat flux (W·m^{-2}), T_s is the soil surface temperature (K), T_a is the air temperature (K), $R_{n,sd}$ is the net radiation flux of the reference soil (W·m^{-2}), G_{sd} is the reference soil heat flux (W·m^{-2}), and T_{sd} is the surface temperature of the reference soil (K).

Submodel of Transpiration of Vegetation

When vegetation completely covers the land surface, soil heat flux G can be ignored, and the reference vegetation canopy temperature (vegetation canopy temperature with zero transpiration) is introduced to calculate vegetation transpiration:

$$\lambda E_c = R_{n,c} - R_{n,cp}\frac{T_c - T_a}{T_{cp} - T_a}, \quad (2)$$

where λE_c is the latent heat flux of transpiration (with λ being the latent heat of the vaporization of water vapor and E_c being the transpiration of vegetation), $R_{n,c}$ is the net radiation of the vegetation canopy (MJ·m-2), T_c is the canopy temperature (℃), T_a is the air temperature (℃), $R_{n,cp}$ is the net radiation flux absorbed by the reference vegetation (MJ·m^{-2}), and T_{cp} is the canopy temperature (℃) of the reference vegetation.

Vegetation-Soil Mixed Zone Model

When the ground surface is a mixed area of vegetation and soil, vegetation coverage is introduced to calculate the total ET by combining the above two submodels:

$$ET = (1 - f) \times E_s + f \times E_c, \quad (3)$$

where f is the fractional vegetation coverage.

Vegetation Index and Fractional Vegetation Cover

The ET inversion of mixed pixels is a difficult point in the application of this model. The normalized difference vegetation index (NDVI) is considered to be the most effective vegetation index for judging whether the underlying surface is a pure pixel. When the NDVI of a pixel is less than or equal to $NDVI_{min}$, the area is a pure soil pixel; when the NDVI of a pixel is greater than or equal to $NDVI_{max}$, the area is a pure vegetation pixel; and when the NDVI is between $NDVI_{min}$ and $NDVI_{max}$, the area is a mixed pixel. Among them, $NDVI_{min}$ and $NDVI_{max}$ represent the NDVI of bare soil and complete vegetation coverage and generally take the mean value of 3% at both ends of the NDVI frequency histogram [42]:

Preprints (www.preprints.org) | NOT PEER-REVIEWED | Posted: 21 June 2023 doi:10.20944/preprints202306.1518.v1

$$NDVI = \frac{NIR - R}{NIR + R}, \tag{4}$$

$$f = \frac{NDVI - NDVI_{\min}}{NDVI_{\max} - NDVI_{\min}}. \tag{5}$$

In the equation, the *NIR* and *R* represent the reflectance of Landsat-8 imagery corresponding to B5 (the NIR band) and B4 (the red band), respectively.

Land Surface Temperature

We used a single-channel algorithm for the inversion of surface temperature [43]:

$$LST = \frac{T_{sensor}}{1 + (\lambda T_{sensor} / A) \ln \varepsilon_0}, \tag{6}$$

where *LST* is the land surface temperature (K); λ is the central wavelength of the thermal infrared band (um); *A* is the product of the Planck constant and the speed of light divided by the Boltzmann constant (the value is 1.439×10^4 um K); T_{sensor} is the brightness temperature (K), which is obtained by direct calibration of the B10 band of the Landsat-8 image; and ε_0 is the surface-specific emissivity.

Net Solar Radiation

The R_n refers to the radiation difference obtained after subtracting the part reflected by the surface from the total solar radiation reaching the surface. It is calculated by Equation (7):

$$R_n = R_{swd} - R_{swu} + R_{lwd} - R_{lwu}, \tag{7}$$

where R_{swd} and R_{swu} represent the absorbed and released shortwave radiation (W m^{-2}), respectively, and R_{lwd} and R_{lwu} represent the absorbed and released longwave radiation (W m^{-2}), respectively. All the above parameters can be obtained by remote sensing inversion.

Soil Heat Flux

Soil heat flux (*G*) is calculated from the relationship between vegetation and net solar radiation:

$$G = R_n[\Gamma_c + (1 - f)(\Gamma_s - \Gamma_c)], \tag{8}$$

where Γ_c and Γ_s are the empirical coefficients, which are respectively 0.05 and 0.315. [44,45].

2.3.3. Timescale Expansion of Evapotranspiration

Satellite remote sensing images can only record instantaneous values at the time of transit, and the ET obtained by 3T model inversion is also an immediate value. In order to understand the actual water consumption during crop growth, daily ET values need to be obtained by extending the transient values on a daily scale. This study used the empirical formula of Jackson et al. [45,46] to extend the instantaneous ET values to daily ET values according to the time-step integration method as follows:

$$ET_d = \frac{2N_e(ET_i)}{\pi \sin(\pi t_i / N_e)}, \tag{9}$$

where ET_d is the daily ET; ET_i is the instantaneous ET; $N_e = N$-2, with *N* being the time interval from sunrise to sunset; and t_i is the time interval from the beginning of the ET process in the early morning to time *i* (the satellite transit time).

2.3.4. Data Analysis

To quantitatively characterize the impact of human activities, an analysis of spatial and temporal variation in ET was conducted using a mask of planting structure classification results, focusing on

Preprints (www.preprints.org) | NOT PEER-REVIEWED | Posted: 21 June 2023 doi:10.20944/preprints202306.1518.v1

two primary crop categories. Meanwhile, the impact of climate on ET variations was characterized through Pearson correlation analysis using spatial interpolation of meteorological factors Ta, P, and VPD. All analyses were pixel based, with a spatial resolution of 30 m.

3. Results

3.1. Crop Identification

To demonstrate that incorporating multitemporal information can enhance classification accuracy, the efficacy of multitemporal information was initially assessed before constructing the classification model. A comparison was conducted between single-temporal, two-temporal, and multitemporal images using a random forest classification model with temporal data from day of year (DOY) 148, DOY164, and DOY244. The findings reveal that the classification accuracy of the multitemporal data combination surpasses that of the single-temporal data combination by 6.93% to 9.53% and exceeds that of the two-temporal data combination by 2.93% to 5.44% (Table 6). Consequently, in subsequent classification Experiments 1 and 2, all classification analyses were performed based on multitemporal images.

Table 6. The overall accuracy of different temporal combinations for crop classification.

Number of Temporal	Date	Overall Accuracy	Kappa Coefficient
1	DOY148	90.00%	0.84
1	DOY164	87.40%	0.79
1	DOY244	89.95%	0.84
2	DOY148, DOY164	91.49%	0.86
2	DOY148, DOY244	92.60%	0.88
2	DOY164, DOY244	94.00%	0.90
3	DOY148, DOY164, DOY244	96.93%	0.95

3.1.1. Classification Experiment 1: Single Band with Multitemporal

In Experiment 1, images from three typical dates representing different crop fertility periods (DOY148, DOY164, and DOY244) were selected for the classification experiment. The accuracy of the results is presented in Figure 4. The results show that the green band has the highest accuracy, while the NIR band's and SWIR-2 band's classification accuracy is lower.

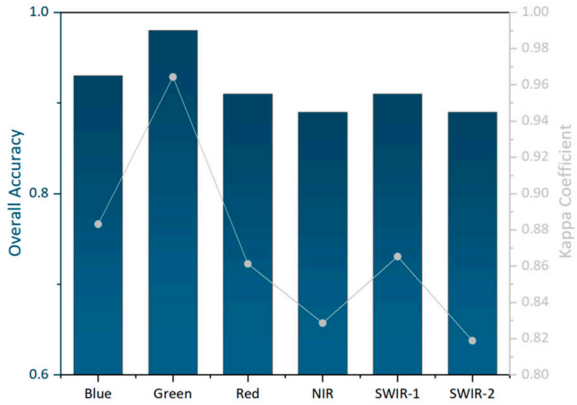

Figure 4. Crop classification accuracy with single-band and multitemporal information.

3.1.2. Classification Experiment 2 : Multi-Band with Multi-Temporal

Figure 5 illustrates the overall accuracy of each band combination, with the abscissa representing the number of bands utilized in each combination. The experimental results reveal that as the number

Preprints (www.preprints.org) | NOT PEER-REVIEWED | Posted: 21 June 2023 doi:10.20944/preprints202306.1518.v1

of bands increases, the highest classification accuracy tends to decrease, while the lowest classification accuracy exhibits an increase. The peak value emerges in the B2 combination, reaching 97.77%. Although the overall accuracy of the B6 combination remains impressive at 96.93%, it does not represent the maximum value. The addition of band information does not effectively enhance classification accuracy.

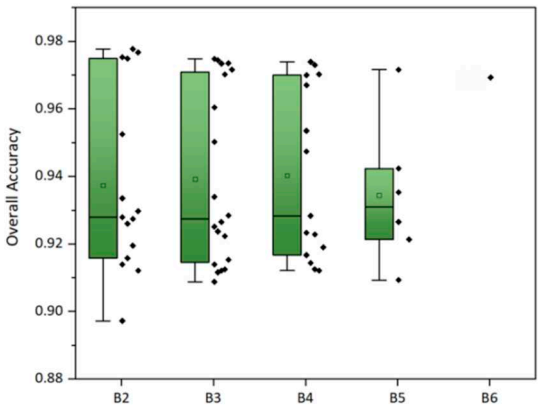

Figure 5. Crop classification's overall accuracy with different band number combinations.

Furthermore, it can be observed that the band combinations achieving the highest classification accuracy consistently include green bands. This finding aligns with the results presented in the single-band multi-temporal, as shown in Table 7. Consequently, the Green and SWIR-1 bands constitute the most sensitive combination for crop classification for the study area.

Table 7. The best band combination of different band combinations for crop classification.

Number of Band Combination	Band of Landsat-8 OLI	Overall Accuracy	Kappa Coefficient
2	Green, SWIR-1	97.77%	0.96
3	Blue, Green, Red	97.48%	0.96
4	Blue, Green, Red, SWIR-2	97.39%	0.96
5	Blue, Green, Red, SWIR-1, SWIR-2	97.16%	0.95
6	Blue, Green, Red, NIR, SWIR-1, SWIR-2	96.93%	0.95

3.1.3. Crop Classification Result in the Liangzhou District

The aforementioned experimental analysis identified a combination of two spectral bands (green and SWIR-1) from three periods (DOY148, DOY164, and DOY244) as the optimal feature set to identify wheat and corn within the study area. The crop distribution map for the LD in 2019 was obtained using the classification model. The evaluation of the confusion matrix for the random forest classification using the optimal feature set is presented in Table 8. The overall accuracy reached 97.77%. To further investigate the interannual adjustments in the planting structure of major crops and elucidate the annual variations in agricultural water consumption, the spatial distribution of wheat and corn in the study area for the year 2020 was extracted using the optimal classification feature set obtained. The results of the planted area for wheat and corn in 2019 and 2020 are presented in Table 9. In 2020, the planted area of wheat was 24.241 kha, which had decreased by 7.353 kha compared to 31.594 kha in 2019. The planted area of corn was 47.322 kha, which had increased by 2.817 hectares compared to 44.505 kha in 2019.

Preprints (www.preprints.org) | NOT PEER-REVIEWED | Posted: 21 June 2023 doi:10.20944/preprints202306.1518.v1

Table 8. Confusion matrix for random forest classification using green and SWIR-1 band combined features.

Crop Types	Classification Results			Total	Producer Accuracy
	Wheat	Corn	Others		
Wheat	646	0	0	646	97.14%
Corn	19	963	29	1011	100.00%
Others	0	0	493	493	94.44%
Total	665	963	522	2150	
User Accuracy	100.00%	85.25%	100		
Overall Accuracy = 97.77% Kappa = 0.96					

Compared with the data in the *Gansu Provincial Statistical Yearbook*, the accuracy of the classification results for wheat in 2019 was 92.58%, the accuracy for corn in 2019 was 98.25%, the accuracy for wheat in 2020 was 85.82%, and the accuracy of corn in 2020 was 96.70%.

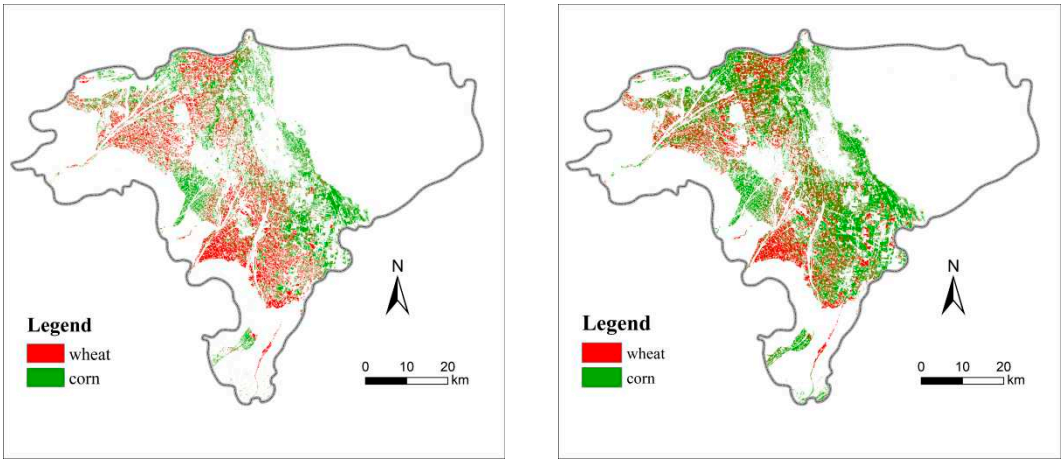

(**a**) (**b**)

Figure 6. Wheat and corn distribution map extracted from Landsat-8 Operational Land Imager (OLI) data in the Liangzhou District (LD): (**a**) is the result for 2019, and (**b**) is the result for 2020.

Table 9. Changes in the wheat and corn planting area in the Liangzhou District (LD) from 2019 to 2020.

Crop Types	2019		2020		Change in Area
	Number of Pixels	Area (kha)	Number of Pixels	Area (kha)	
Wheat	351221	31.594	269483	24.241	-7.353
Corn	494747	44.505	526061	47.322	2.817
Total	845968	76.099	795544	71.563	-4.536

3.2. Evapotranspiration Estimation

3.2.1. Key Model Parameters Inversion

The input parameters of the 3T model were inverted for typical dates of the different growth stages (for May 12, May 28, June 13, and September 1, 2019), resulting in the spatial distribution of parameters such as the NDVI and LST based on crop mask extraction.

The distribution diagrams for the NDVI highlight the distinctions in phenological stages among different crops (Figures 7 and 8). On May 12, the NDVI values in the wheat region were primarily

Preprints (www.preprints.org) | NOT PEER-REVIEWED | Posted: 21 June 2023 doi:10.20944/preprints202306.1518.v1

distributed between 0.5 and 0.7, while the NDVI values in the corn region were below 0.4. Over time, the NDVI values exhibited a gradual increase. On June 13, the wheat flourished, with the NDVI value reaching approximately 0.8. By September 1, the wheat had been harvested, and the NDVI in the original wheat distribution area had diminished. Concurrently, the corn area reached a peak of 0.95.

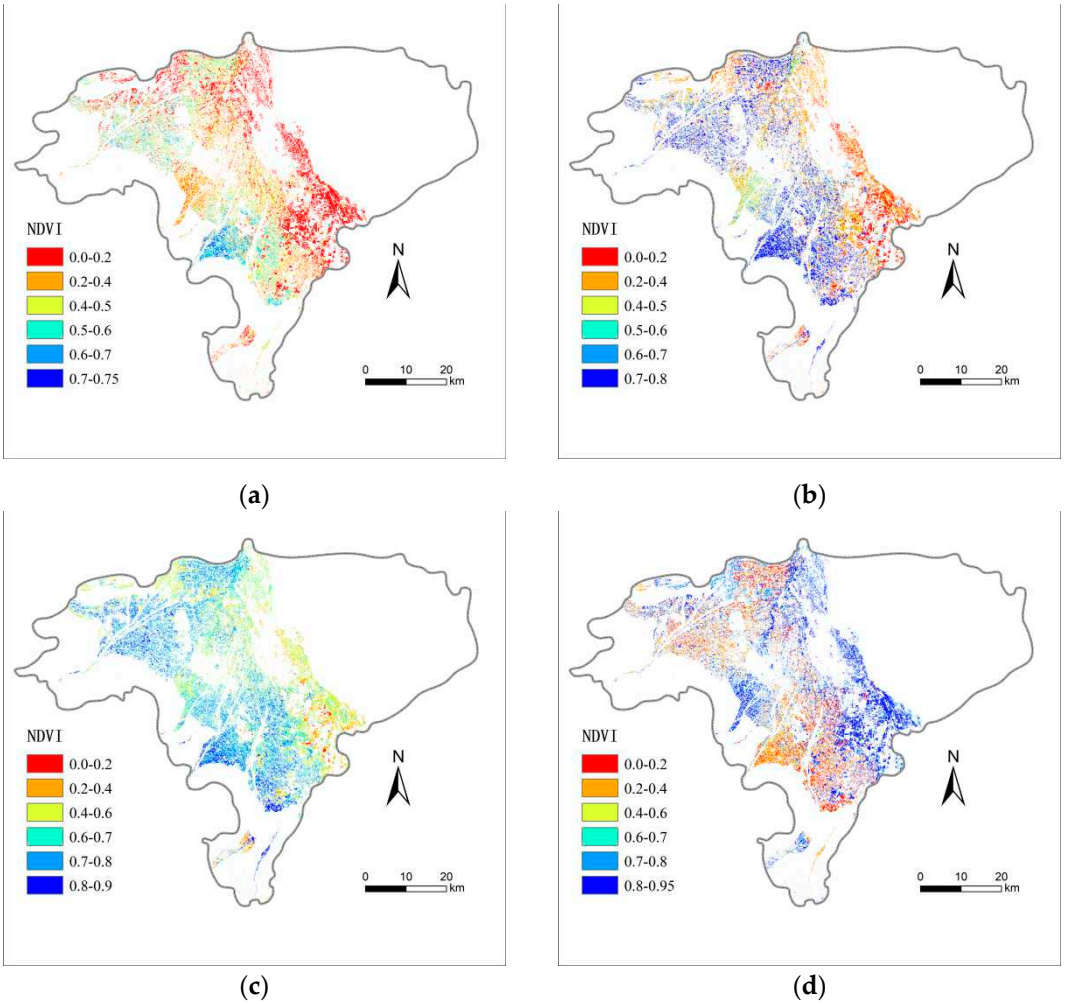

Figure 7. Inversion results for the normalized difference vegetation index (NDVI): (**a**) is the result from May 12, 2019; (**b**) is the result from May 28, 2019; (**c**) is the result from June 13, 2019; and (**d**) is the result from September 1, 2019.

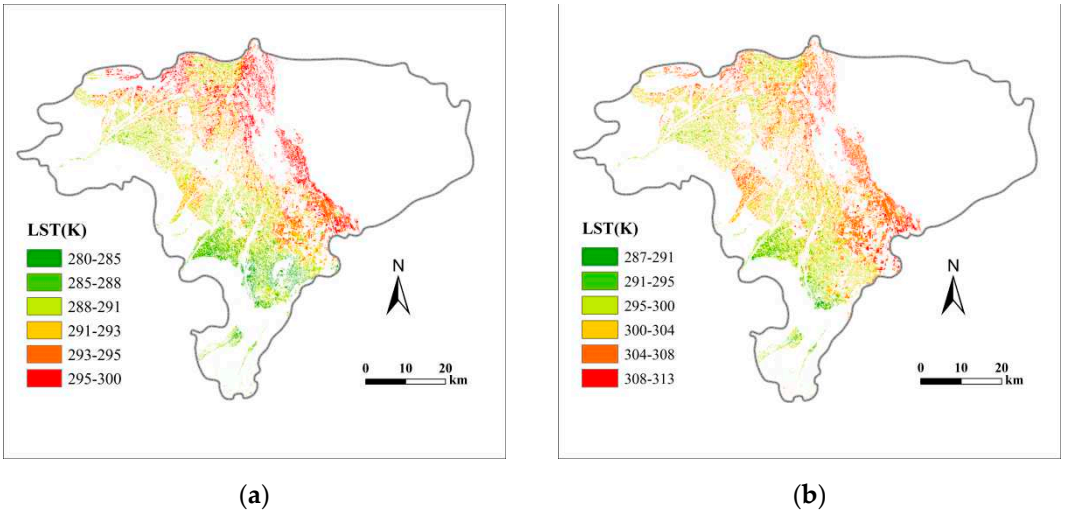

Preprints (www.preprints.org) | NOT PEER-REVIEWED | Posted: 21 June 2023 doi:10.20944/preprints202306.1518.v1

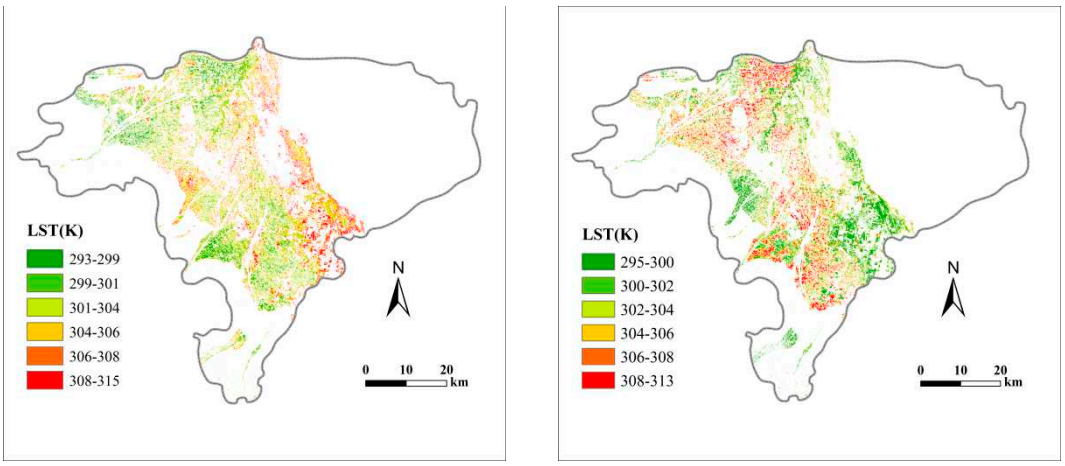

(**c**) (**d**)

Figure 8. Inversion results for the land surface temperature (LST): (**a**) is the result from May 12, 2019; (**b**) is the result from May 28, 2019; (**c**) is the result from June 13, 2019; and (**d**) is the result from September 1, 2019.

The LST exhibited pronounced spatial heterogeneity and is strongly correlated with vegetation coverage. In areas with low vegetation coverage, the temperature is higher due to the exposed surface. For example, in Changcheng town (102°54′, 37°54′), which is surrounded by desert, the LST remained elevated throughout the entire crop growth period, with the lowest value at 295 K and the highest value reaching 315 K. During these four periods, the wheat region showed lower LSTs than corn, mainly due to the influence of the leaf morphology of the two plants.

3.2.2. Variation of Evapotranspiration

Figures 12 and 13 depict the instantaneous ET obtained by substituting each parameter from the inversion into the 3T model, as well as the daily values of ET acquired through the daily scale expansion of ET as proposed by Jackson et al. [37,46]. Significant spatial and temporal heterogeneity exists in the ET values across the region. The ET frequencies (Figures 9 and 10e) reveal that the peak of the ET curve shifted backward with crop growth and approached a bimodal shape in each period, with the two peaks representing the wheat and corn zones, respectively. During May and June, ET was higher in the wheat distribution area, with the phenomenon being most pronounced in June. The daily ET peaks on May 28 and June 13 were 2.4 mm/d and 4.0 mm/d, and 2.0 mm/d and 5.2 mm/d, respectively. The left peak represents ET in the corn zone, while the right peak represents ET for wheat.

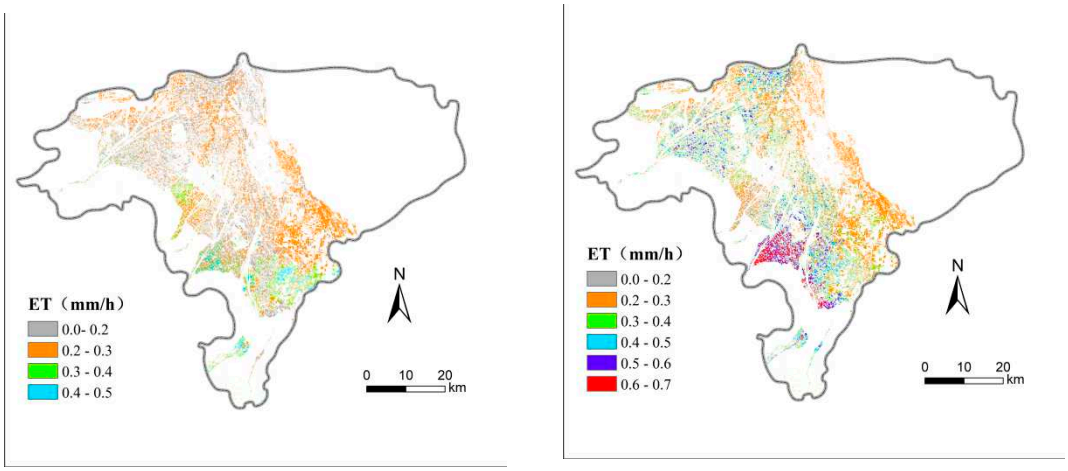

(**a**) (**b**)

Preprints (www.preprints.org) | NOT PEER-REVIEWED | Posted: 21 June 2023 doi:10.20944/preprints202306.1518.v1

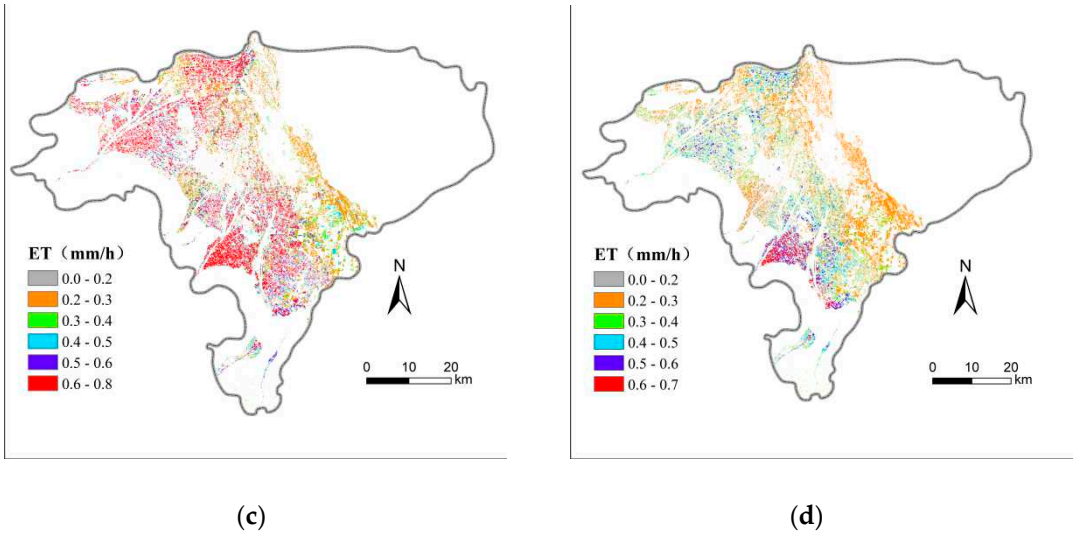

(**c**) (**d**)

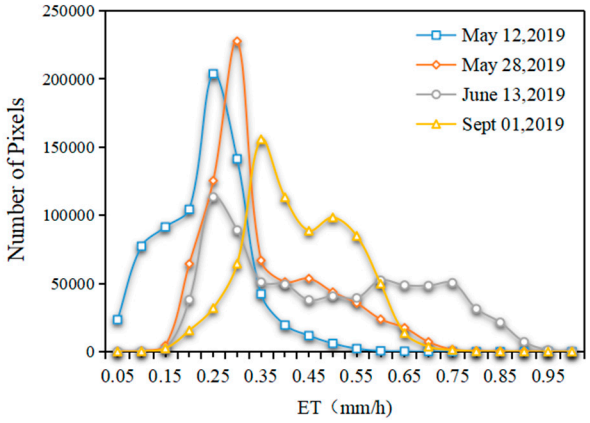

(**e**)

Figure 9. Inversion results for evapotranspiration (ET, mm/h): (**a**) is the result from May 12, 2019; (**b**) is the result from May 28, 2019; (**c**) is the result from June 13, 2019; (**d**) is the result from September 1, 2019; and (**e**) represents the instantaneous ET frequency map in each period.

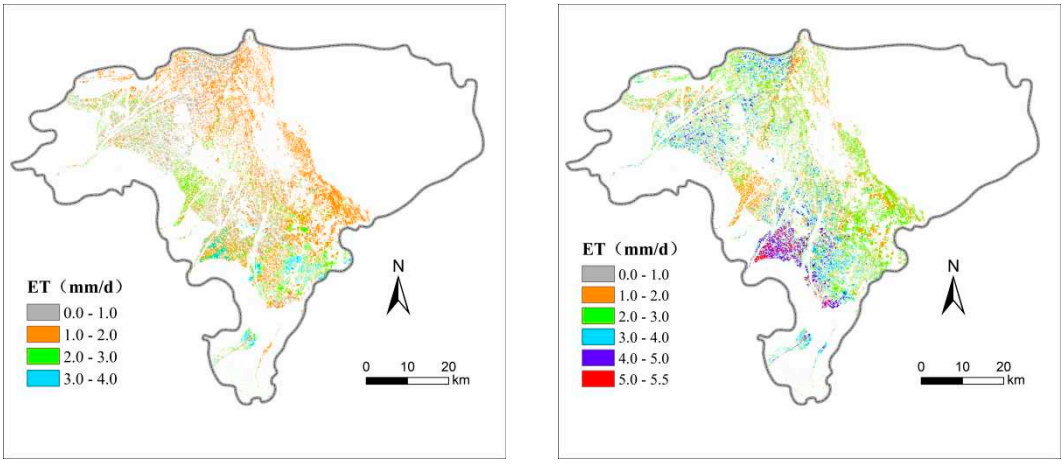

(**a**) (**b**)

Preprints (www.preprints.org) | NOT PEER-REVIEWED | Posted: 21 June 2023 doi:10.20944/preprints202306.1518.v1

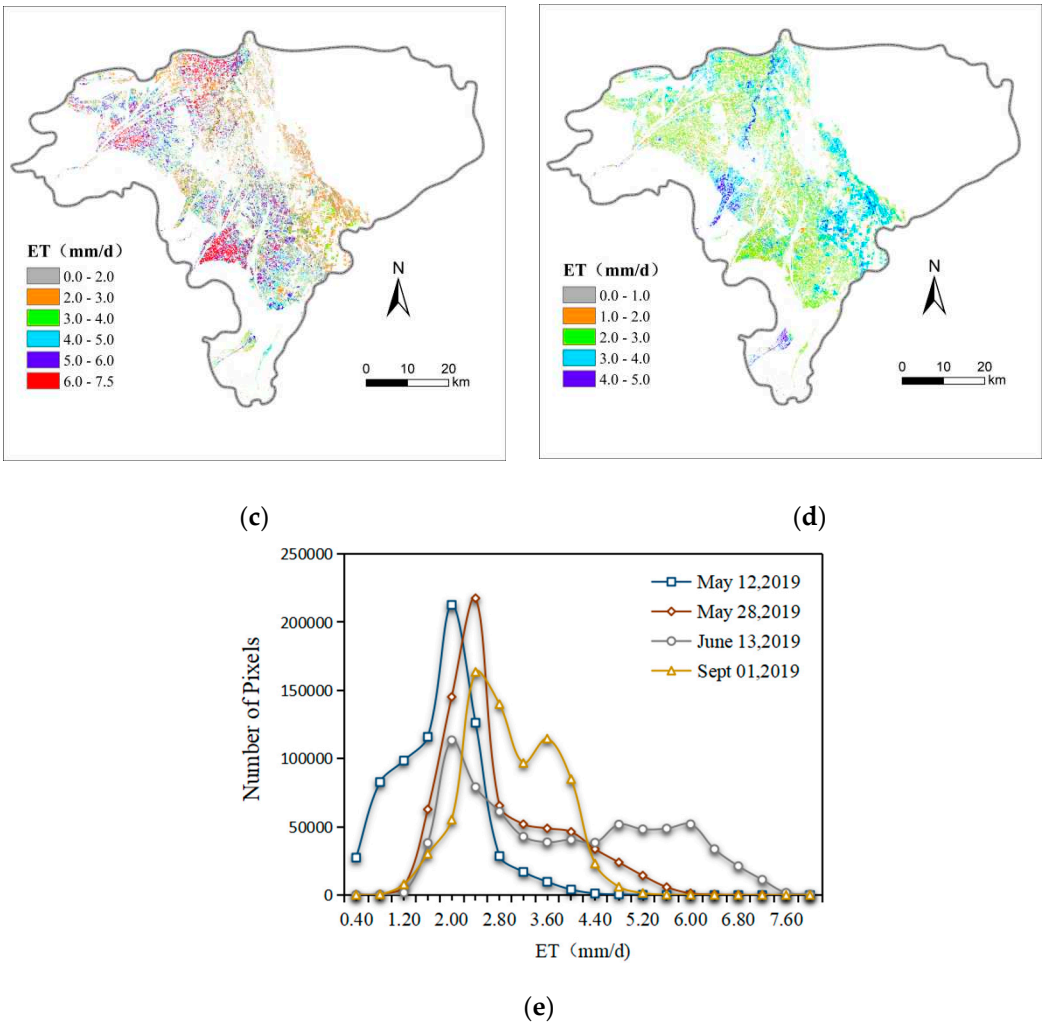

Figure 10. Inversion results for evapotranspiration (ET, mm/d): (a) is the result from May 12, 2019; (b) is the result from May 28, 2019; (c) is the result from June 13, 2019; (d) is the result from September 1, 2019; and (e) represents the frequency of daily ET in each period.

Figure 11 presents images from the same period in 2020, selected to illustrate the interannual variation of ET. The model parameters were obtained in the same manner and substituted into the 3T model to derive the daily ET values on June 24, 2020. This reveals an overall decrease in daily crop ET, with a maximum value of 4.0 mm/d compared to June 13, 2019. This decrease is significantly correlated with the later fertility of wheat and maize in 2020 as opposed to 2019. However, ET levels increased in the maize range compared to 2019, and the effects of changes in climatic factors such as temperature must be taken into account. Consequently, the following analysis examines the primary factors affecting ET in terms of both climate change and human activities.

Preprints (www.preprints.org) | NOT PEER-REVIEWED | Posted: 21 June 2023 doi:10.20944/preprints202306.1518.v1

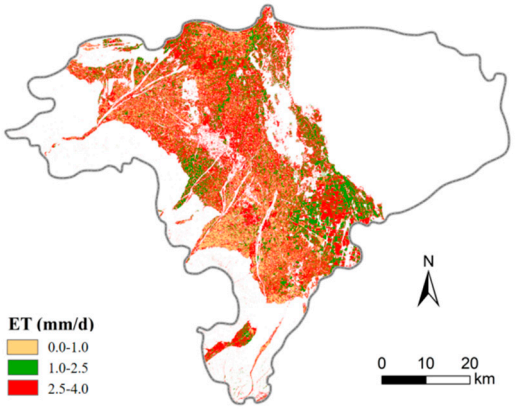

Figure 11. Daily evapotranspiration (ET) results for June 24, 2020.

3.3. The Response of Evapotranspiration to Planting Structure Factors

In order to better understand the difference in emission caused by different crop types in each period, the study extracted wheat and corn areas for mask analysis. Significant spatial heterogeneity is observed in the ET of both wheat and maize, which correlates with the NDVI and LST.

The spatial distribution in May is significantly different. The daily ET value of the wheat area was 0.4–2.0 mm/d on May 12 and 2.0–5.5 mm/d on May 28. The difference in spatial distribution decreased in June, and the ET of the whole area was relatively concentrated. The daily ET on June 13 was 4.2–7.2 mm/d. According to the time distribution characteristics, the wheat ET increased from May to June and showed a gradual deepening of color from the spatial distribution map. On May 12, May 28, and June 13, the average daily ET in the study area was 1.16 mm/d, 3.44 mm/d, and 5.02 mm/d respectively.

In May, the spatial difference in ET distribution in the corn area is slight compared with the wheat area. On May 12, the daily ET value of the corn area was 1.5~2.5 mm/d, and the value was 1.5~2.6 mm/d on May 28. In June and September, the spatial difference increased. The daily ET in the corn area was 1.5~4.0 mm/d on June 13 and 2.0~4.4 mm/d on September 1. On May 12, May 28, June 13, and September 1, the average daily ET of corn in the study area was 1.87 mm/d, 2.03 mm/d, 2.8 mm/d, and 3.2 mm/d, respectively. From the frequency distribution plots, it can be observed that both wheat and corn exhibit a rightward shift in their peak values over time. Additionally, there are notable differences in ET among different crops during the same period, which can effectively distinguish them. The findings considering the crop structure provide a scientific basis for precise irrigation.

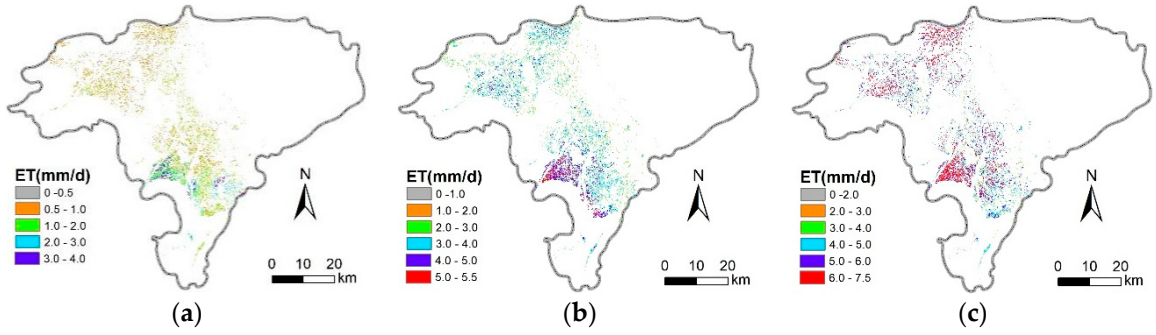

Preprints (www.preprints.org) | NOT PEER-REVIEWED | Posted: 21 June 2023 doi:10.20944/preprints202306.1518.v1

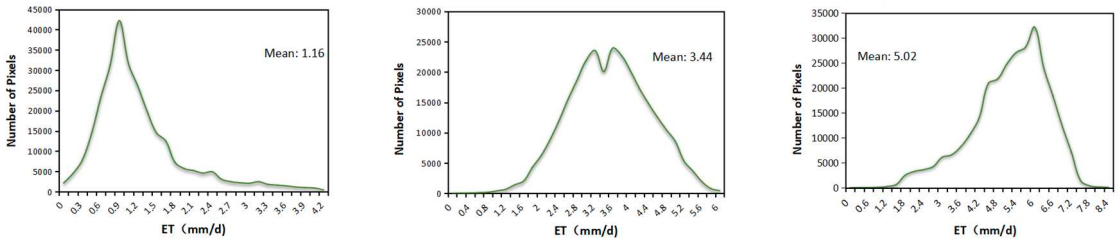

(**d**) (**e**) (**f**)

Figure 12. Daily evapotranspiration (ET) extracted by mask in the wheat area (mm/d): (**a**) is the result from May 12, 2019; (**b**) is the result from May 28, 2019; and (**c**) is the result from June 13, 2019. Since the wheat was harvested in September, no date from the month is analyzed here. Finally, (**d**–**f**) represent the frequency of daily ET on the corresponding dates.

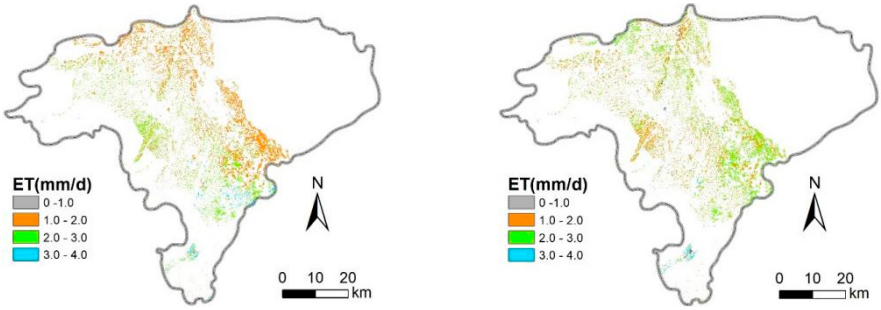

(**a**)

(**b**)

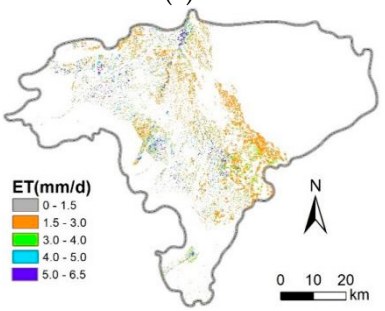

(**c**)

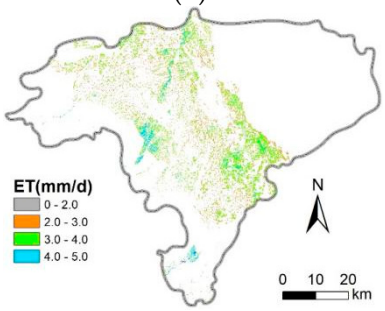

(**d**)

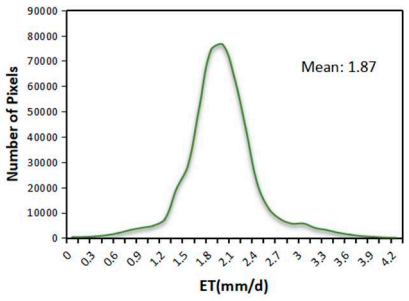

(**e**)

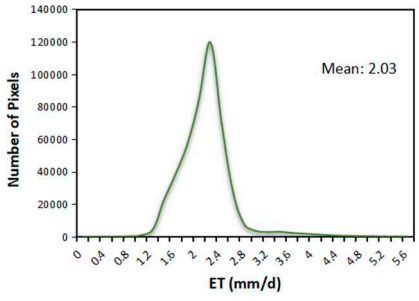

(**f**)

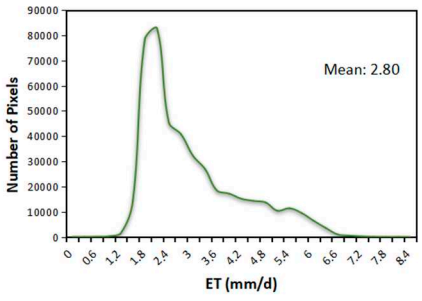

(**g**)

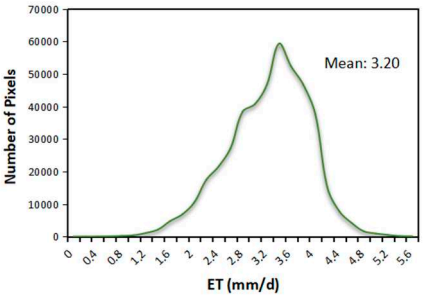

(**h**)

Preprints (www.preprints.org) | NOT PEER-REVIEWED | Posted: 21 June 2023 doi:10.20944/preprints202306.1518.v1

Figure 13. Daily evapotranspiration (ET) extracted by mask in the corn area (mm/d): (a) is the result from May 12, 2019; (b) is the result from May 28, 2019; (c) is the result from June 13, 2019; (d) is the result from September 1, 2019; and (e), (f), (g), and (h) represent the frequency of daily ET on the corresponding dates.

3.4. The Response of Evapotranspiration to Climatic Factors

The Pearson correlation analysis was conducted using the remotely sensed ET obtained during the typical days of the crop growing seasons in 2019 and 2020 and the corresponding climatic factors of the respective years (Figure 14). From the results of the color-coded correlation matrices for interannual variation, it can be seen that Ta is the main factor affecting the change in ET and the correlation reaches 0.80 (R = 0.80, p < 0.05). Moreover, P also has a certain impact on ET, but the correlation is only 0.57 (R = 0.57, p < 0.05). This is because the agricultural fields in the study area are irrigated croplands, where crop growth relies entirely on artificial irrigation. Additionally, the study area is located in the Shiyang River Basin, which is characterized by limited and highly localized precipitation. Meanwhile, the correlation between the VPD and ET was only 0.21 (R = 0.21), which is consistent with the findings of Jin et al. [25]. They observed that VPD has only a slight influence on transpiration, while solar radiation plays a dominant role in atmospheric exchanges and serves as the primary driving force behind the spatial distribution of ET.

Figure 14. The color-coded correlation matrices for ET interannual variation.

4. Discussion

4.1. The Influence of Input Spectral Bands on the Inversion of Planting Structures

The choice of spectral bands for the satellite inversion of planting structures in watersheds should depend on several factors, including the resolution and availability of data, the types of crops being analyzed, and the goals of the analysis. Our results suggest that a more efficient band combination can improve the inversion accuracy of crop classification. The evidence indicates that combining the green and SWIR-1 bands is often a practical choice for the inversion of cropping structures in a watershed [47].

The green band is sensitive to chlorophyll and leaf area, providing information on the vegetation cover and its structure. The SWIR-1 band, on the other hand, is sensitive to the water and structural properties of vegetation, providing information on the water content and structure of the canopy [48–50]. Such a combination of bands can provide more practical information about vegetation and water content and is a crucial input for the inversion of planting structures. Meanwhile, increasing the number of bands or features in the classification does not necessarily improve the classification accuracy. Prior researchers have found that the information redundancy between variables increases

 doi:10.20944/preprints202306.1518.v1

the computational complexity and limits any improvement in accuracy, which is consistent with our findings [51].

4.2. The Influence of the Spatial Heterogeneity of Planting Structures on Evapotranspiration

In agriculturally complex regions with diverse planting structures, higher spatial and temporal resolution inputs are needed to study the dynamic variations of water-use efficiency factors, such as ET [52]. In many irrigated agricultural areas, different crops are staggered and the fields are irregular and fragmented, resulting in sharp spatial fluctuations in parameters such as ET, soil moisture, and LST [28]. Most existing inversion models neglect the physiological characteristics arising from significant differences in water conditions among different crops [53–55]. According to the results of the planting structure analysis, the planted area of major cash crops decreased by 4.536 kha in 2020 compared to 2019, which contributed to the reduction in ET in 2020. From the input parameters of the 3T model, notable differences in key ET inversion features were observed between wheat and corn. In May and June, wheat exhibited higher ET levels in its distribution area due to being in the middle to late stages of the growth period, with a maximum vegetation coverage of 1.0. Meanwhile, corn was still in the early stage of the elongation period in mid-June, with a plant height ranging from 0.8 to 1.0 meters. Wheat in the LD is harvested around July 20, after which the wheat area is fallowed or rotated with crops such as baby bok choy by September 1 while corn reaches its maturity stage. At this time, corn exhibits the highest levels of ET throughout its growth period, with a daily value of 3.6 mm/d. These results emphasize the importance of crop species' influence on ET inversion and quantitative characterization. More importantly, the findings demonstrate the significance of conducting crop classification with remote sensing inversion for crop moisture status monitoring.

In section 3, as a representative crop of typical crops with significant differences in water consumption, we performed a mask analysis for the wheat and maize zones, respectively, and found that the ET inversion results were most influenced by the crop type based on the image element properties. However, the ET distribution of wheat and maize in different periods is distributed in all zones, and the proportion is more pronounced (more pixels, > 5000), so there are errors in the inversion results. Two main factors are causing the errors: first, there are some discrepancies between the wheat and maize planting structure extracted from the remote sensing images and the field planting situation, and the fragmented plots that do not belong to both have been mistakenly identified as well. Second, due to the limitation of the resolution of Landsat-8 data, there is a phenomenon of mixed pixels, and the inversion results of the fragmented plots will have errors compared to the actual values. Therefore, the values with a more concentrated frequency were selected when analyzing the inversion results for practical application. The anomalous marginal values were discarded to reduce the interference of the anomalous values.

4.3. The Influence of Meteorological Factors on the Inversion of Evapotranspiration

In the arid area of Northwest China, high ET is caused by high temperatures and low humidity. Ta is a relatively stable environmental factor, and this study considers it as the main meteorological factor influencing the spatiotemporal variation of ET. The increase in temperature promotes the evaporation rate of soil moisture from the crop surface and the topsoil, resulting in more water entering the atmosphere through faster evaporation. In the study conducted by Jun et al. [56] in Lanzhou, the meteorological factors considered were net radiation, air temperature, and relative humidity. Their results reveal a significant relationship between air temperature and crop evapotranspiration, with an R^2 of 0.789. Meanwhile, Gao's study indicates a strong correlation between temperature variations and field ET during the crop growth period, with a coefficient of determination exceeding 0.9 [57]. In addition, Rigden et al. [58] demonstrated that on longer time scales, variations in precipitation among meteorological factors had the most prominent impact on the partitioning of ET. The changes in soil moisture resulting from P also exerted a significant influence on ET. Precipitation also affected ET, but the correlation was lower (about 0.57). A typical feature of the Shiyang River Basin is low precipitation, and the precipitation events are highly localized, especially in the crop-growing season. ET is influenced by precipitation because it

replenishes soil moisture. However, for the irrigated farmland in the LD, the supply of precipitation is far from sufficient to support crop growth.

5. Conclusions

Planting structure identification in the LD was investigated in this study using multispectral and multitemporal Landsat-8 images. A novel quantitative characterization of the response of ET to climate and planting structure changes was achieved, and the detailed conclusions indicate the following:

（1）The accuracy of planting structure identification can be improved by efficiently selecting spectral information. Using a random forest classifier, a combination of the green and SWIR-1 bands from multitemporal Landsat-8 images was found to be the optimal feature set to extract the planting structures in the LD. The wheat planting areas in the study area were 31.594 kha and 24.241 kha in 2019 and 2020, respectively, while the corn areas were 44.505 kha and 47.322 kha for those same years. The accuracy of the planting structure classification results ranged from 85.82% to 98.25%.

（2）After considering the spatial heterogeneity of the crop planting structure, the accuracy of the inversion results for the model input parameters such as NDVI and LST significantly improved. The integration of crop planting structure with the 3T model enhanced the realism and reliability of ET inversion.

（3）Concerning the climatic factors considered in this study, ET's spatiotemporal variations were primarily driven by Ta ($R = 0.80$, $p \leq 0.05$). The research quantified the contributions of changes in crop planting structure and climatic factors to variations in ET, providing a basis for better understanding the impact of crop planting structure on remote sensing-based ET estimation. However, this study focused on major cash crops, and further exploration is needed to investigate the effects of more refined and diverse crop planting structures on ET using remote sensing techniques.

Author Contributions: Conceptualization, X.Y., X.S.,Y.Z. and F.T.; data curation, X.S. and F.T.; formal analysis, X.Y. and X.S.; funding acquisition, F.T.; investigation, X.Y., X.S.and Y.Z.;

methodology, X.Y., X.S.,Y.Z. and F.T.; project administration, F.T.; software, X.Y.; supervision, F.T. and S.O.-F.; validation, X.Y., X.S.,Y.Z. and F.T.; visualization, X.Y.; writing—original draft, X.Y.; writing—review and editing, F.T. All authors have read and agreed to the published version of the manuscript.

Funding: This work was supported by the National Natural Science Foundation of China (52179049),the international and regional cooperation and exchange projects of the National Natural Science Foundation of China (51961125205), and National Agency for Research and Development (ANID)/PCI(NSFC190013), the financial support provided by the National Key R&D Program of China (2022YFD190050403) and *Western Light* -Key Laboratory Cooperative Research Cross-Team Project of Chinese Academy of Sciences(xbzg-zdsys-202103).

Data Availability Statement: Not applicable.

Conflicts of Interest: All the authors declare no conflict of interest.

References

1. Liu, J.; You, Y.; Li, J.; Sitch, S.; Gu, X.; Nabel, J.E.M.S.; Lombardozzi, D.; Luo, M.; Feng, X.; Arneth, A.; *et al.*. Response of global land evapotranspiration to climate change, elevated CO2, and land use change. *Agric. For. Meteorol.* **2021**, 311, 108663.
2. Wei, Z.; Yoshimura, K.; Wang, L.; Miralles, D.G.; Jasechko, S.; Lee, X. Revisiting the contribution of transpiration to global terrestrial evapotranspiration. *Geophys. Res. Lett.* **2017**, 44, 2792-801.
3. Kool, D.; Agam, N.; Lazarovitch, N.; Heitman, J.L.; Sauer, T.J.; Ben-Gal, A. A review of approaches for evapotranspiration partitioning. *Agric. For. Meteorol.* **2014**, 184, 56-70.
4. SOER, G.J.R. Estimation of Regional Evapotranspiration and Soft Moisture Conditions Using Remotely Sensed Crop Surface Temperatures. *Remote Sens Environ*. **1980**, 9, 27-45.
5. QIU, G.; MOMII, K.; YANO, T. Estimation of Plant Transpiration by Imitation Leaf Temperature Theoretical consideration and filed verfication(I）. *Trans. Jpn. Soc. Irrig. Drain. Reclam. Eng.* **1996**, 183, 401-10.

6. Qiu, G.; Wang, S.; Wu, X. Three Temperature (3T) Model——A Method to Estimate Evapotranspiration and Evaluate Environmental Quality. *J. Plant Ecol.* **2006**, 30, 231-8.
7. Tian, F.; Qiu, G.; Yang, Y.; Lü, Y.; Xiong, Y. Estimation of evapotranspiration and its partition based on an extended three-temperature model and MODIS products. *J. Hydrol.* **2013**, 498, 210-20.
8. Xiong, Y.; Zhao, S.; Tian, F.; Qiu, G. An evapotranspiration product for arid regions based on the three-temperature model and thermal remote sensing. *J. Hydrol.* **2015**, 530, 392-404.
9. Hou, M.; Tian, F.; Zhang, L.; Li, S.; Du, T.; Huang, M.; Yuan, Y. Estimating Crop Transpiration of Soybean under Different Irrigation Treatments Using Thermal Infrared Remote Sensing Imagery. *Agronomy*. **2019**, 9, 8.
10. Piao, S.; Friedlingstein, P.; Ciais, P.; de Noblet-Ducoudré, N.; Labat, D.; Zaehle, S. Changes in climate and land use have a larger direct impact than rising CO_2 on global river runoff trends. *Proceedings of the National Academy of Sciences - PNAS*. **2007**, 104, 15242-7.
11. Zhang, Y.; Qiu, G.; Yan, C.; Wen, H. Studies on the influence of altitudes on the trend of reference evapotranspiration in recent 50 years: a case study of Sichuan province. *Ecology and Environmental Sciences*. **2018**, 27, 2208-16.
12. Qiu, M.; Liu, B.; Liu, Y.; Zhang, Y.; Wu, X.; Yuan, F.; Wang, D.; Mu, C. Temporal -Spatial Variation Characteristics of Reference Crop Evapotranspiration and Its Influence Factors in Jilin Province. *J. Arid Environ.* **2019**, 37, 119-26.
13. Li, Y.; Zhang, L.; Cao, Y. Spatiotemporal variation characteristics of potential evapotranspiration and climate influencing factors in Hebei province. *South-to-North Water Transfers and Water Science & Technology*. **2019**, 17, 67-78.
14. Liu, X.; Zheng, H.; Zhang, M.; Liu, C. Identification of dominant climate factor for pan evaporation trend in the Tibetan Plateau. *J. Geogr. Sci.* **2011**, 21, 594-608.
15. Jin, Z.; Liang, W.; Yang, Y.; Zhang, W.; Yan, J.; Chen, X.; Li, S.; Mo, X. Separating Vegetation Greening and Climate Change Controls on Evapotranspiration trend over the Loess Plateau. *Sci Rep*. **2017**, 7.
16. He, G.; Zhao, Y.; Wang, J.; Gao, X.; He, F.; Li, H.; Zhai, J.; Wang, Q.; Zhu, Y. Attribution analysis based on Budyko hypothesis for land evapotranspiration change in the Loess Plateau, China. *J. Arid Land*. **2019**, 11, 939-53.
17. Bolton, D.K.; Friedl, M.A. Forecasting crop yield using remotely sensed vegetation indices and crop phenology metrics. *Agric. For. Meteorol.* **2013**, 173, 74-84.
18. KANG, S. Towards water and food security in China. *Chinese Journal of Eco-Agriculture*. **2014**, 880-5.
19. Yang, F.; Matsushita, B.; Yang, W.; Fukushima, T. Mapping the human footprint from satellite measurements in Japan. *Isprs-J. Photogramm. Remote Sens.* **2014**, 88, 80-90.
20. Chen, H.; Qiu, Y.; Yin, D.; Chen, J.; Chen, X.; Liu, S.; Liu, L. Stacked spectral feature space patch: An advanced spectral representation for precise crop classification based on convolutional neural network. *The Crop Journal*. **2022**, 10, 1460-9.
21. Biradar, C.M.; Xiao, X. Quantifying the area and spatial distribution of double- and triple-cropping croplands in India with multi-temporal MODIS imagery in 2005. *Int. J. Remote Sens.* **2011**, 32, 367-86.
22. Dong, J.; Xiao, X.; Menarguez, M.A.; Zhang, G.; Qin, Y.; Thau, D.; Biradar, C.; Moore, B. Mapping paddy rice planting area in northeastern Asia with Landsat 8 images, phenology-based algorithm and Google Earth Engine. *Remote Sens. Environ.* **2016**, 185, 142-54.
23. Gao, F.; Anderson, M.C.; Zhang, X.; Yang, Z.; Alfieri, J.G.; Kustas, W.P.; Mueller, R.; Johnson, D.M.; Prueger, J.H. Toward mapping crop progress at field scales through fusion of Landsat and MODIS imagery. *Remote Sens. Environ.* **2017**, 188, 9-25.
24. Wardlow, B.D.; Egbert, S.L. Large-area crop mapping using time-series MODIS 250 m NDVI data: An assessment for the U.S. Central Great Plains. *Remote Sens. Environ.* **2008**, 112, 1096-116.
25. Xiao, X.; Boles, S.; Liu, J.; Zhuang, D.; Frolking, S.; Li, C.; Salas, W.; Moore, B. Mapping paddy rice agriculture in southern China using multi-temporal MODIS images. *Remote Sens. Environ.* **2005**, 95, 480-92.
26. Konduri, V.S.; Kumar, J.; Hargrove, W.W.; Hoffman, F.M.; Ganguly, A.R. Mapping crops within the growing season across the United States. *Remote Sens. Environ.* **2020**, 251, 112048.
27. You, N.; Dong, J. Examining earliest identifiable timing of crops using all available Sentinel 1/2 imagery and Google Earth Engine. *Isprs-J. Photogramm. Remote Sens.* **2020**, 161, 109-23.

28. Wang, S.; Wang, C.; Zhang, C.; Xue, J.; Wang, P.; Wang, X.; Wang, W.; Zhang, X.; Li, W.; Huang, G.; *et al.*. A classification-based spatiotemporal adaptive fusion model for the evaluation of remotely sensed evapotranspiration in heterogeneous irrigated agricultural area. *Remote Sens. Environ.* **2022**, 273, 112962.
29. Mankin, J.S.; Seager, R.; Smerdon, J.E.; Cook, B.I.; Williams, A.P. Mid-latitude freshwater availability reduced by projected vegetation responses to climate change. *Nat. Geosci.* **2019**, 12, 983-8.
30. Chintala, S.; Harmya, T.S.; Kambhammettu, B.V.N.P.; Moharana, S.; Duvvuri, S. Modelling high-resolution Evapotranspiration in fragmented croplands from the constellation of Sentinels. *Remote Sensing Applications: Society and Environment*. **2022**, 26, 100704.
31. Tran, K.H.; Zhang, H.K.; McMaine, J.T.; Zhang, X.; Luo, D. 10 m crop type mapping using Sentinel-2 reflectance and 30 m cropland data layer product. *Int. J. Appl. Earth Obs. Geoinf.* **2022**, 107, 102692.
32. Wardlow, B.D.; Egbert, S.L.; Kastens, J.H. Analysis of time-series MODIS 250 m vegetation index data for crop classification in the U.S. Central Great Plains. *Remote Sens. Environ.* **2007**, 108, 290-310.
33. Duro, D.C.; Franklin, S.E.; Dubé, M.G. A comparison of pixel-based and object-based image analysis with selected machine learning algorithms for the classification of agricultural landscapes using SPOT-5 HRG imagery. *Remote Sens. Environ.* **2012**, 118, 259-72.
34. Cai, Y.; Guan, K.; Peng, J.; Wang, S.; Seifert, C.; Wardlow, B.; Li, Z. A high-performance and in-season classification system of field-level crop types using time-series Landsat data and a machine learning approach. *Remote Sens. Environ.* **2018**, 210, 35-47.
35. Zhong, L.; Gong, P.; Biging, G.S. Efficient corn and soybean mapping with temporal extendability: A multi-year experiment using Landsat imagery. *Remote Sens. Environ.* **2014**, 140, 1-13.
36. Zhong, L.; Hu, L.; Zhou, H. Deep learning based multi-temporal crop classification. *Remote Sens. Environ.* **2019**, 221, 430-43.
37. Xiong, J.; Thenkabail, P.S.; Gumma, M.K.; Teluguntla, P.; Poehnelt, J.; Congalton, R.G.; Yadav, K.; Thau, D. Automated cropland mapping of continental Africa using Google Earth Engine cloud computing. *Isprs-J. Photogramm. Remote Sens.* **2017**, 126, 225-44.
38. Chen, M.; Li, C.; Guan, Y.; Zhou, J.; Wang, D.; Luo, Z. Generation and application of high temporal and spatial resolution images of regional farmland based on ESTARFM model. *Acta Agronomica Sinica*. **2019**, 45, 1099-110.
39. Qiu, G.Y.; Yano, T.; Momii, K. An improved methodology to measure evaporation from bare soil based on comparison of surface temperature with a dry soil surface. *J. Hydrol.* **1998**, 210, 93-105.
40. Lu, S.; Xuan, J.; Zhang, T.; Bai, X.; Tian, F.; Ortega-Farias, S. Effect of the Shadow Pixels on Evapotranspiration Inversion of Vineyard: A High-Resolution UAV-Based and Ground-Based Remote Sensing Measurements. *Remote Sens.* **2022**, 14, 2259.
41. Tian, F.; Qiu, G.; Lü, Y.; Yang, Y.; Xiong, Y. Use of high-resolution thermal infrared remote sensing and "three-temperature model" for transpiration monitoring in arid inland river catchment. *J. Hydrol.* **2014**, 515, 307-15.
42. WALTHALL, C. A comparison of empirical and neural network approaches for estimating corn and soybean leaf area index from Landsat ETM+ imagery*1. *Remote Sens. Environ.* **2004**, 92, 465-74.
43. ARTIS, D.A.; CARNAHAN, W.H. Survey of Emissivity Variability in Thennography of Urban Areas. *Remote Sens. Environ.* **1982**, 12, 313-29.
44. Monteith, J.L. Solar Radiation and Productivity in Tropical Ecosystems. *J. Appl. Ecol.* **1972**, 9, 747-66.
45. Kustas, W.P.; Daughtry, C.S.T. Estimation of the soil heat flux/net radiation ratio from spectral data. *Agric. For. Meteorol.* **1990**, 49, 205-23.
46. Jackson, R.D.; Hatfield, J.L.; Reginato, R.J.; Idso, S.B.; Jr. Pinter, P.J. Estimation of daily evapotranspiration from one time-of-day measurements. *Agric. Water Manage.* **1983**, 7, 351-62.
47. Hively, W.D.; Lamb, B.T.; Daughtry, C.S.T.; Serbin, G.; Dennison, P.; Kokaly, R.F.; Wu, Z.; Masek, J.G. Evaluation of SWIR Crop Residue Bands for the Landsat Next Mission. *Remote Sens.* **2021**, 13, 3718.
48. Yilmaz, M.T.; Hunt, E.R.; Jackson, T.J. Remote sensing of vegetation water content from equivalent water thickness using satellite imagery. *Remote Sens. Environ.* **2008**, 112, 2514-22.
49. Feng, S.; Zhao, J.; Liu, T.; Zhang, H.; Zhang, Z.; Guo, X. Crop Type Identification and Mapping Using Machine Learning Algorithms and Sentinel-2 Time Series Data. *Ieee J. Sel. Top. Appl. Earth Observ. Remote Sens.* **2019**, 12, 3295-306.
50. Ghulam, A.; Li, Z.; Qin, Q.; Yimit, H.; Wang, J. Estimating crop water stress with ETM+ NIR and SWIR data. *Agric. For. Meteorol.* **2008**, 148, 1679-95.

51. Camps-Va, G.; Mooij, J.; Scholkopf, B. Remote Sensing Feature Selection by Kernel Dependence Measures. *Ieee Geosci. Remote Sens. Lett.* **2010**, 7, 587-91.
52. Kang, S.; Su, X.; Tong, L.; Shi, P.; Yang, X.; YukuoAbe; Du, T.; Shen, Q.; Zhang, J. The impacts of human activities on the water – land environment of the Shiyang River basin, an arid region in northwest China / Les impacts des activités humaines sur l ' environnement pédo- hydrologique du bassin de la Rivière Shiyang, une région aride du nord-ouest de la Chine. *Hydrol. Sci. J.-J. Sci. Hydrol.* **2004**, 49, 413-27.
53. Bastiaanssen, W.G.M.; Menenti, M.; Feddes, R.A.; Holtslag, A.A.M. A remote sensing surface energy balance algorithm for land (SEBAL). 1. Formulation. *J. Hydrol.* **1998**, 212-213, 198-212.
54. Norman, J.M.; Kustas, W.P.; Humes, K.S. Source approach for estimating soil and vegetation energy fluxes in observations of directional radiometric surface temperature [Agric. For. Meteorol., 77 (1995) 263 – 293]. *Agric. For. Meteorol.* **1996**, 80, 297.
55. Long, D.; Singh, V.P. A modified surface energy balance algorithm for land (M-SEBAL) based on a trapezoidal framework. *Water Resour. Res.* **2012**, 48.
56. Jun, D. Studies on Stomatal Conductance and Evapotranspiration of Maize Field in Semi-arid Area., Vol. Master:Lanzhou University, 2017.
57. Gao, H. Water and energy Balance of irrigated Field in the Middle Basis oasis of Heihe River., Vol. PhD thesis:The University of Chinese Academy of Sciences, 2015.
58. Rigden, A.J.; Salvucci, G.D.; Entekhabi, D.; Short Gianotti, D.J. Partitioning Evapotranspiration Over the Continental United States Using Weather Station Data. *Geophys. Res. Lett.* **2018**, 45, 9605-13.